New Journal of Physics
The open access journal at the forefront of physics

Deutsche Physikalische Gesellschaft DPG
IOP Institute of Physics

Published in partnership with: Deutsche Physikalische Gesellschaft and the Institute of Physics

OPEN ACCESS

RECEIVED
27 March 2022

REVISED
1 July 2022

ACCEPTED FOR PUBLICATION
7 July 2022

PUBLISHED
9 August 2022

PAPER

Water jet space charge spectroscopy: route to direct measurement of electron dynamics for organic systems in their natural environment

Michael Mittermair[1], Felix Martin[1], Martin Wörle[1], Dana Bloß[2], Andreas Duensing[1], Reinhard Kienberger[1], Andreas Hans[2], Hristo Iglev[1,*], André Knie[2,*] and Wolfram Helml[3,*]

[1] Physik Department E11, Technische Universität München, James-Franck-Str. 1, D-85748 Garching, Germany
[2] Institut für Physik und CINSaT, Universität Kassel, Heinrich-Plett-Straße 40, D-34132 Kassel, Germany
[3] Fakultät Physik, Technische Universität Dortmund, Maria-Goeppert-Mayer-Str. 2, D-44227 Dortmund, Germany
[*] Authors to whom any correspondence should be addressed.

E-mail: higlev@ph.tum.de, knie@physik.uni-kassel.de and wolfram.helml@tu-dortmund.de

Keywords: ultrashort, liquid microjet, electron dynamics

Supplementary material for this article is available online

Abstract

The toolbox for time-resolved direct measurements of electron dynamics covers a variety of methods. Since the experimental effort is increasing rapidly with achievable time resolution, there is an urge for simple and robust measurement techniques. Within this paper prove-of-concept experiments and numerical simulations are utilized to investigate the applicability of a new setup for the generation of ultrashort electron pulses in the energy range of 300 eV up to 1.6 keV. The experimental approach combines an in-vacuum liquid microjet and a few-cycle femtosecond laser system, while the threshold for electron impact ionization serves as a gate for the effective electron pulse duration. The experiments prove that electrons in the keV regime are accessible and that the electron spectrum can be easily tuned by laser intensity and focal position alignment with respect to the water jet. Numerical simulations show that a sub-picosecond temporal resolution is achievable.

1. Introduction

Over the past years the concepts for the observation of fundamental processes connected with electron reconfiguration dynamics in real time have been developed continuously [1–3]. Better encryption of these dynamics would lead to a more direct understanding based on the changes of the underlying electron configuration, and open the opportunity to generate and control desired properties and reaction pathways in a deliberate and efficient manner [4–7]. Naturally, for these pioneering experiments the objects of investigation have been chosen to be as simple as possible to demonstrate the potential of new ultrafast methods and fully develop their capabilities in a well-understood setting. Thus, while the temporal resolution of table-top experimental systems has been improved from picoseconds to femtoseconds and attoseconds, the systems under investigation were continuously becoming less complex—from chemical reactions in molecules and transient dynamics at metal surfaces to excitation and relaxation processes in the most basic systems like the helium [8] and hydrogen atom [9–11].

Now that our understanding of these techniques has ripened and grown, we are on the brink of broadening the range of ultrafast research again to practically more relevant subjects like the internal charge separation in solar cells [12, 13], efficient current control in electronic materials [14, 15] or the bondbreaking and re-structuring in biomolecules [16, 17].

An area of very high interest is the complex of open questions surrounding damage of DNA molecules following UV radiation or electron impact [18–20]. This has consequences for cancer radiation therapy

[21, 22], the problem of skin burn by sun light and the effects of secondary radiation on organic cells in a technologically quickly evolving world [23, 24].

Since all those biologically relevant reactions occur within human cells and thereby basically in liquid solution, there is an undeniable requirement for a robust tabletop technique, which is capable of probing organic molecules in a liquid environment while maintaining ultrashort time resolution. We want to pave the road for a new technique that satisfies these needs.

2. Methods

2.1. A new method for generating ultrashort electron pulses

In solid-state photoemission experiments the so-called spacecharge effect, where the repellent Coulomb force acting between electrons escaping from the surface, is an unwanted but permanent companion [25]. While such a cloud of electrons is obstructive in photoemission experiments, we see a chance to exploit it as an ultrashort source of electrons with kinetic energies in the keV region.

There already are experiments about generating electrons from a liquid jet using ultrashort laser pulses. As reported, electrons with kinetic energies of up to 300 keV were generated by creating a plasma at the jet surface [26]. Furthermore, it was shown that these electrons induce K-shell vacancies, which leads to emission of characteristic K_α radiation in a secondary metal target [27].

While in [27] the generation of x-ray radiation was at the center of research, we concentrate on the electrons. The idea is to utilize the electrons themselves as an *in situ* probe for samples dissolved in the liquid jet. This allows us to spare the secondary metal target, increasing the efficiency of the process and to simplify the experimental scheme.

We propose a novel experimental apparatus consisting of a liquid microjet combined with a titanium-sapphire laser system, which delivers bandwidth-limited few-cycle laser pulses. These ultrashort laser pulses generate a cloud of free electrons in the gaseous vicinity of the liquid jet as schematically shown in figure 1. The electrons within the cloud experience repulsion due to the Coulombic interaction, which eventually leads to expansion of the cloud. While the inner electrons feel the repelling force from all sides, which does not allow them to gain much kinetic energy, the outer ones feel the pushing force from the cloud and gain the highest kinetic energy. These fastest electrons, which can be referred to as cutoff electrons, build an expanding shell which is followed by a trail of slower electrons. In 1991, Ammosov derived a straightforward formula to describe the behavior of the fastest electrons by applying the energy conservation law for an expanding sphere of electrons [28]:

$$\frac{1}{4\pi\varepsilon_0}\frac{Ne^2}{r_0} = \frac{1}{4\pi\varepsilon_0}\frac{Ne^2}{r} + \frac{m_e v^2}{2} \tag{1}$$

with the electron mass m_e, charge e and electron velocity v. N is the number of uniformly distributed electrons inside a sphere of radius r_0 generated at $t = 0$. The electron kinetic energy for very large radii of the expanding shell ($r \to \infty$) is given by $E_{\mathrm{kin}} = Ne^2/4\pi\varepsilon_0 r_0$. These electrons from the surrounding water vapor will be emitted in all directions from their place of origin. In particular, a certain quota of the fast electrons will hit the liquid jet and interact with water molecules or any species of organic compound dissolved inside the liquid.

The basic idea behind the experiment is to use the fastest electrons, which inherently emerge within an extremely narrow time window, as pump or probe in a time-resolved experiment. As only the fastest electrons have sufficient energy to ionize a core level electron, the element specific threshold for electron impact ionization can be used to distinguish between fast and slow ones. By keeping the high-energy shoulder of the electron spectrum just above the threshold, an electron pulse with an ultrashort effective pulse duration can be achieved. Biologically relevant molecules morstly consist of carbon, nitrogen and oxygen with their K-shell ionization thresholds at 296 eV, 406 eV and 543 eV, respectively [29–31].

2.2. Experimental details

2.2.1. The laser system

All measurements were performed with a commercial master oscillator (Femtosource™ Rainbow™) power amplifier (Femtopower™HEHR CEP4) system. The pulses were spectrally broadened in a home-built differentially pumped hollow-core fiber setup and temporally compressed within a chirped-mirror array. The pulse length was optimized for maximum cutoff energy. This laser system delivers pulses with an energy of up to 1.5 mJ and a pulse length shorter than 5 fs at a repetition rate of 4 kHz. The laser wavelength is centered at 690 nm with a linear polarization. A more detailed description of the system can be found in [32, 33].

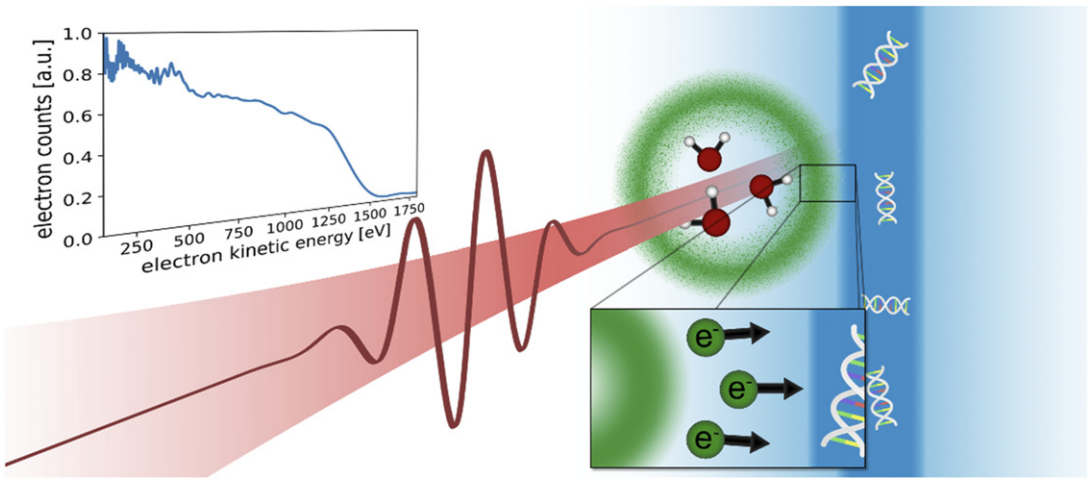

Figure 1. Novel scheme for ultrafast studies of electron impact in liquid water. An ultrashort laser pulse (red) generates a cloud of free electrons in the surrounding gas phase of a liquid microjet (blue). The charged cloud (green) expands due to the repelling Coulomb force. Thereby, the outermost electrons experience the highest acceleration creating a shell of high-energy electrons followed by a trail of slower ones. Discriminating between fast and slow electrons allows for exploitation of this ultrashort bunch of fast electrons. These electrons will eventually hit the liquid microjet and can be utilized to examine dissolved organic molecules, e.g., DNA, in their natural environment.

2.2.2. The liquid microjet

The liquid microjet was produced by injecting water with a high-performance liquid chromatography (HPLC) pump through a 25 μm-sized glass nozzle into the vacuum. A flow of 0.8 ml min^{-1} required 8 bar backing pressure. Adjustment by a 3D-manipulator system allowed for fine tuning of the distance between water jet and laser pathway. After interaction with the laser beam, the jet was collected by a cryogenic cold trap, cooled with liquid nitrogen from outside the vacuum. With a second cold trap in the interaction chamber a pressure of 10^{-2} mbar in the interaction region and 10^{-5} mbar in the electron spectrometer was maintained, ensuring proper operation of the electron detector. A depiction of the vacuum setup can be found in the supplement. The jet was operated at room temperature and grounded outside the vacuum via a gold wire connected to the liquid near the vacuum feedthrough to prevent charging of the liquid and the nozzle. A low concentration (50 mM max.) of NaCl was added to the water solution for the same reason.

2.2.3. The time-of-flight spectrometer

All spectra were recorded with an *ETF11* electron time-of-flight spectrometer from *Stefan Käsdorf Geräte für Forschung und Industrie*. The spectrometer is designed to work under high-vacuum conditions below 10^{-6} mbar and has an entrance aperture of 3 mm. With the backing pressure in a liquid microjet experiment being way higher than in solid state experiments, it was necessary to reduce this aperture to ensure proper vacuum conditions inside the drift tube. This is achieved by implementing a custom made 170 μm pinhole which reduces the aperture and thereby the gas flow by a factor of about 400. Electrons are measured in a direction perpendicular to the laser polarization, mostly preventing direct observation of electrons accelerated by above-threshold ionization (ATI) [33]. For readout a *Teledyne LeCroy Waverunner 104 MXI* oscilloscope is used.

3. Results

3.1. Proof-of-principle experiments

To establish the feasibility of this new approach it is required to clarify two aspects. Foremost, one needs to show that the electron acceleration by the charged cloud is strong enough to create electrons with a kinetic energy higher than the respective element-specific threshold for electron impact ionization. Secondly, scrutinizing the time structure of the electron bunch is necessary to demonstrate the applicability of this approach for ultrafast spectroscopy experiments. From equation (1) we know that the final kinetic energy of the electrons is linked to the expansion of the charge cloud. Therefore, it is obligatory to examine the relation between the initial distance between the electron cloud and the liquid microjet, which sets the effective radius of the expanded charge cloud. The distance between laser focus and liquid jet is varied by the manipulator system keeping all other parameters constant. Figure 2 shows how the kinetic energy

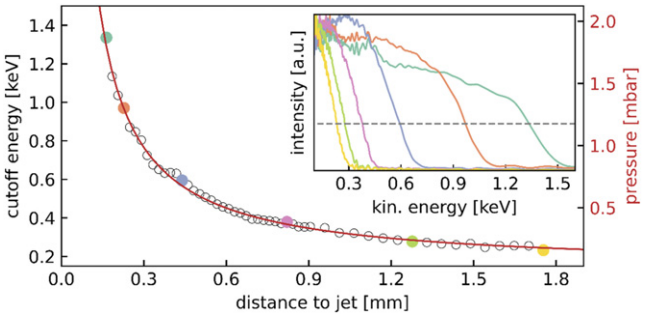

Figure 2. Cutoff kinetic energy versus distance between laser focus and liquid microjet. Circles show experimental data for the cutoff energy (left scale) and determined gas pressure (right scale). The inlay shows the corresponding experimental photoelectron spectra. The grey dashed line in the inlay marks the cutoff threshold. The red line shows the radial pressure dependence as given by equation (2). The cutoff energy dependence on the gas density validates the assumption of a collective acceleration mechanism.

cutoff, which is defined as the energy where the signal intensity drops to 30% of its plateau value, changes with the distance between the liquid microjet and the laser focus.

With the cutoff energy being proportional to the number of generated free electrons as shown in equation (1), it is obviously proportional to the number of molecules at the laser focus and thereby to the gas pressure. According to Faubel *et al* [34], the radial pressure dependency in a liquid microjet experiment follows the rule for a cylindrical particle source

$$p(R) = \frac{R_0}{R} p_0 \quad \text{for } (R > R_0) \tag{2}$$

with radial distance R, the equilibrium pressure at the liquid surface $p_0 = 23.4$ mbar at a liquid temperature of 20 °C and the jet radius R_0 of 12.5 μm. It is possible to fit

$$E_{\text{cutoff}}(R) = \frac{A}{R - R_C} + B \tag{3}$$

to the data. Here, the center of the liquid jet is represented by R_C. A is a constant scaling factor, which takes into account the size of the initial electron cloud and the ionization probability per water molecule. In general the effective density of free electrons depends on various parameters like the ionization cross section and laser intensity as well as the evaporation rate of the microjet and the initial size of the laser focus. From comparison of equations (3) and (2) it follows that $E_{\text{cutoff}} \propto p(R) + B$ within the observed pressure range. The parameter B is a linear offset, which is needed for the fit to match the data. Physically it might originate from electrons which have been accelerated in the laser field instead of acceleration by the charged electron cloud. From the known distance between laser focus and jet it is possible to determine the gas pressure for every measured spectrum, following the red line in figure 2. One can see that the electrons reach kinetic energies in the keV regime which is sufficiently high to introduce inner shell vacancies (K-shell) in light elements up to magnesium. Notably, these elements play an extraordinary role when it comes to biological relevant molecules. The initial electron cloud is generated via laser induced ionization of the water vapor. For high laser intensities the distinction between multiphoton and tunneling/barrier suppression ionization is given by the Keldysh adiabaticity parameter [35]

$$\gamma = \omega \frac{\sqrt{2 m_e I_p}}{e\mathcal{E}}, \tag{4}$$

with the frequency of the driving laser ω, the ionization potential $I_p = 12.6$ eV of the $1b_1$ molecular orbital of water [36, 37] and the laser field strength $\mathcal{E}$. The maximum intensity calculated from the applied laser parameters and focus conditions reaches up to 1.3×10^{17} W cm^{-2}, which corresponds to a maximum field strength $\mathcal{E}_{\text{max}} = 1 \times 10^{12}$ V m^{-1}, leading to $\gamma = 0.033$, a clear indicator that tunneling or barrier suppression ionization is dominant. These regimes are separated by the barrier-suppression field strength $\mathcal{E}_{\text{bsi}}$, which marks the condition where the atomic ionization potential and the effective one-dimensional potential barrier are equal assuming a constant electric field [38]

$$\mathcal{E}_{\text{bsi}} = \frac{I_p^2}{4Z}, \tag{5}$$

where Z is the charge of the remaining ion [39]. Thus, with the electric field $\mathcal{E}_{\text{max}}$ clearly exceeding the barrier suppression limit $\mathcal{E}_{\text{bsi}} = 5.3 \times 10^{10}$ V m^{-1} for the weakest bound electrons multiple electron

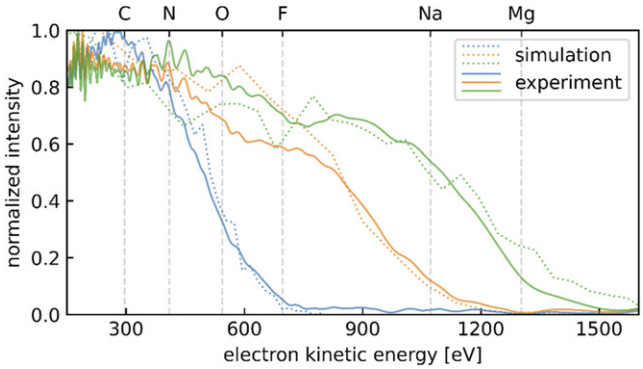

Figure 3. Comparison of the experimental electron spectra and simulated results. The solid lines represent the experimental data for laser intensities of approximately 2.6×10^{16} W cm^{-2} (blue), 4.5×10^{16} W cm^{-2} (orange), and 5.3×10^{16} W cm^{-2} (green). The simulated spectra are represented as dashed lines in corresponding colors. In the simulations electron clouds of 300 (blue), 500 (orange) and 700 (green) million electrons have been assumed. To classify the cutoff energies achieved, the *K*-shell binding energies of selected elements are plotted on the upper abscissa.

ionization is likely to occur. At the high intensity employed in the experiment, also the Lorentz force comes into play, which further alters the single-electron dynamics [40]. The magnetic field of the laser pulse influences the trajectories of the fast ATI electrons, which reduces their probability of recollision with the corresponding parent ion and thus their contribution to the measured spectra.

In order to link the experimental results with the underlying mechanisms, a Monte Carlo simulation based on classical transport theory was implemented. It includes the electron acceleration by the electric field of the laser as well as the influence of the space charge effect due to the high density of generated free electrons. The simulation was divided into two consecutive parts: the first part handles the ionization process and the electron acceleration in the electric field of the laser pulse. It also takes into account elastic and inelastic scattering events with the surrounding water molecules. The second part addresses the space charge effect harnessing the charge distribution from the first part as a starting point.

3.2. Modeling space charge acceleration

To reach applicability in ultrafast science it is necessary to examine the time structure of the electron pulses and to validate that the electrons reach those energies before they hit the liquid jet surface. For this purpose we employ a two stage Monte Carlo simulation. After a time of about 11 fs, the influence of the amplitude of the laser electric field can be neglected and the space charge effect becomes the dominant acceleration mechanism. Due to their large density, the free electrons strongly repel each other and are therefore accelerated. However, this acceleration is partially suppressed by the positively charged water ions originating from the ionization process. To estimate the electric field generated by the positively charged ions, a mean field approach has been chosen. Since the positively charged ions are much heavier than the electrons, they can be assumed to remain stuck at their initial position throughout the whole acceleration process. Therefore, a homogeneously charged cylinder of water ions is assumed. In order to reduce computational effort the space within and around this cylinder is divided into segments. The electrons from the first simulation are assigned to these segments and their kinematic features, collective mass and charge, as well as, position and velocity are averaged. The introduction of these 'pseudo-electrons' drastically reduces the number of simulated particles and therefore the spent calculation time.

Figure 3 compares the simulation results with experimental data. The solid lines show electron spectra for laser intensities of 2.6×10^{16} W cm^{-2} (blue), 4.5×10^{16} W cm^{-2} (orange), and 5.3×10^{16} W cm^{-2} (green). One can observe how the spectra shift towards higher energies with increasing laser intensity. The dashed lines represent the results from a set of simulations that only differ in the total number of ionized electrons N. The simulations are selected to fit the high-energy cutoff of the corresponding experimental spectra, with the kinetic energy being calculated from the velocity component pointing towards the detector.

We find excellent agreement in the high-energy cutoff. The slow electrons, which do not have sufficient energy to liberate an electron from an inner shell, deviate from the quantitative prediction and are not part of the further considerations. To classify the cutoff energies achieved, the *K*-shell binding energies of selected elements are plotted on the upper abscissa in figure 3.

For demonstration, we take a closer look onto the 300 million particle simulation (blue dashed line in figure 3). Figure 4(A) shows the energy and spatial evolution of the simulated electron cloud for a series of instances in time. Again, we only take into account the contribution to the kinetic energy by the velocity in

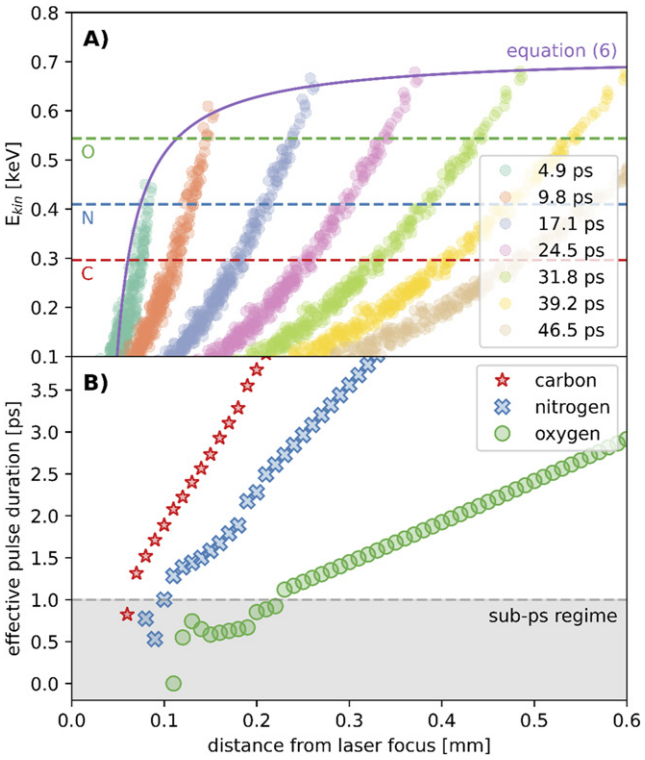

Figure 4. Temporal and spatial evolution of the simulated electron cloud. (A) Electron kinetic energy distributions into the direction of the detector for different instants in time from 5 ps to 50 ps. The solid purple line represents the highest kinetic energy over time and arises from fitting equation (6). The dashed lines mark the energy thresholds for K-shell ionization in carbon (red), nitrogen (blue), and oxygen (green). (B) The full-width at half maximum of the effective electron pulse duration versus its distance to the origin of the electron cloud for carbon (red stars), nitrogen (blue crosses), and oxygen (green circles). For calculation of the effective pulse duration only electrons with a kinetic energy above the threshold for the associated K-shell ionization are taken into account.

the direction towards the detector. The purple line shows a fit of the fastest electrons by

$$E_{\mathrm{kin}}(r) = \frac{Ne^2}{4\pi\varepsilon_0}\left(\frac{1}{r_0} - \frac{1}{r}\right) \tag{6}$$

which is a rearranged version of equation (1). One can see that the electrons gain most of their kinetic energy within the first 200 μm.

The dashed lines mark the K-shell ionization thresholds for carbon (red), nitrogen (blue), and oxygen (green). Figure 4(B) shows the derived effective electron pulse duration versus the distance to the center of the electron cloud. The effective duration is calculated as the full-width at half maximum of the temporal distribution for electrons with kinetic energy above the respective K-shell ionization threshold. The pulse shape linearly disperses with distance, whereby a threshold closer to the electron cutoff allows for smaller dispersion as well as for shorter pulse duration.

4. Discussion

As noted in the introduction, there is a growing demand for investigating organic molecules in their natural liquid environment with an ultrashort time resolution. Obviously, it is a significant step to reduce the requirements for these measurements usually conducted in large-scale facilities to a tabletop technique. We tackle this by combining an in-vacuum liquid microjet with an ultrafast laser system, capitalizing on the ever present space charge effect. The extremely small distance between the origin of the electrons and their experimental utilization allows the electron pulse to stay confined during acceleration. As driving mechanism for the electron acceleration the Coulombic repulsion due to space charge within a cloud of electrons is exploited. The necessary ultrashort electron pulse duration is achieved by selecting the threshold for electron impact ionization of inner shells in the target elements in combination with the experimentally adjustable time-energy distribution of the electron cloud as temporal gate.

Varying the distance between laser focus and liquid microjet provides a parameter that can be used to efficiently tune the resulting electron spectrum. With kinetic energies in the low keV regime we

demonstrated that electron impact ionization of core holes is accessible, which is the most important necessity that must be met to allow this technique to work. The applied numerical model reproduces the experimental data remarkably well, which implies that the simulation depicts the acceleration mechanism sufficiently in detail. The extracted temporal and spatial evolution of the fast electrons shows that the electrons gain most of their kinetic energy within a very short distance from their origin. The effective electron pulse duration is calculated for a set of exemplary atomic species, demonstrating that a duration shorter than 1 ps can be achieved.

The interaction region where the electron cloud hits the liquid jet is limited by the distance between jet and laser focus. Since the electron density decreases proportionally to the square of the distance, the interaction region (defined as full width at half maximum) is limited to two times the distance between jet and focus (cf supplement figure S3 (https://stacks.iop.org/NJP/24/073040/mmedia)). Furthermore, the large scattering cross-section for electrons with kinetic energies of about 1 keV in liquid water limits their penetration depth below 50 nm. The small interaction region facilitates relatively high electron densities and makes pump-probe experiments possible without the need of further electron optics.

5. Conclusion

Our work lays the foundation for a new experimental technique relying on space charge-driven electrons as a direct in-situ excitation source for ultrafast measurements in liquids. To complete the scheme also a mechanism suited for probing the ionized molecules has to be implemented. The most promising one is to detect the characteristic K_α radiation using an energy-dispersive Si-photodiode as in [27] or a suitable grating spectrometer. Another possibility is the detection of the element-specific Auger electrons employing a high-resolution detector like a hemispherical electron energy analyzer. This would also have the added benefit of observing electrons at different emission angles, thus providing an additional handle on the experimental parameters and allowing to study the potential influence of rescattered high-energy ATI electrons. Since it is already present in the water jet, oxygen offers a great first test case for the detection scheme. In a next step, sodium chloride could be added to the liquid jet. By varying the concentration of sodium ions, which have accessible K-shell binding energy, one can investigate the sensitivity for dissolved specimen before turning towards biological samples. Thus, a versatile, affordable and compact experimental setup is made available for studies on biologically relevant systems in their natural environment.

Acknowledgments

This research was supported by the Deutsche Forschungsgemeinschaft (DFG) via the Cluster of Excellence 'e-conversion' EXC 2089/1-390776260.

Data availability statement

The data that support the findings of this study are available upon reasonable request from the authors.

Appendix A

A.1. Simulation of ionization and acceleration in the electric field

The time dependent electron release profile at high laser intensities as they are employed in the experiment can be estimated using the ADK-theory described by Corkum *et al* [33]:

$$\Gamma(t) \propto \frac{1}{\mathrm{E}_0 f(t)} \exp\left[-\frac{2}{3}\left(\frac{I_\mathrm{p}}{I_\mathrm{h}}\right)^{\frac{3}{2}} \frac{1}{\mathrm{E}_0 f(t)}\right], \tag{7}$$

where I_p and I_h represent the ionization potentials of water $1\mathrm{b}_1$ and hydrogen $\mathcal{E}_0$ is the amplitude of the electric field while $f(t)$ accounts for its time dependence. Spatially, the electrons are assumed to be emitted in a cylinder with its diameter corresponding to the laser beam's estimated waist diameter of about 50 μm and the axial dimension set to 11 cm well above the Rayleigh length of the laser beam. According to classical transport theory, the electron trajectory in an electric field can be described by a differential equation (in

Hartree atomic units) of the form:

$$\ddot{x} = \dot{v} = \frac{\mathrm{d}^2 x}{\mathrm{d}t^2} = a = -\mathrm{E}, \tag{8}$$

with the position vector x, the velocity vector v, the acceleration vector a, the electric field vector $\mathcal{E}$ and the time t. The equation of motion can be solved numerically by applying a so-called Leapfrog algorithm, where the calculation of the position and the velocity happens at interleaved time points which have a distance of half the time step unit dt. For integer time steps dt with index i, it can be expressed as:

$$x_{i+1} = x_i + v_i\,\mathrm{d}t + \frac{1}{2}a_i\,\mathrm{d}t^2 \tag{9}$$

and

$$v_{i+1} = v_i + \frac{1}{2}(a_i + a_{i+1})\mathrm{d}t. \tag{10}$$

At each time step there is a certain possibility for a scattering event to take place, which is derived from elastic and inelastic scattering cross section. For an assumed ambient water pressure of 1 mbar however, scattering events of electrons with surrounding water molecules during the excursion in the laser electric field can be neglected. This simplification is justified for electrons with kinetic energy above 50 eV, which have a total scattering cross section smaller than 10×10^{-16} cm^2 [41]. With a pressure of 1 mbar and a temperature of 296 K, this yields a mean free path of 385 μm, which clearly exceeds the length scale on which the electric field accelerates the electrons.

ORCID iDs

Michael Mittermair https://orcid.org/0000-0001-8794-3084
Reinhard Kienberger https://orcid.org/0000-0001-8781-3685
Andreas Hans https://orcid.org/0000-0002-4176-4766
Hristo Iglev https://orcid.org/0000-0001-9208-0068
André Knie https://orcid.org/0000-0002-2208-8838
Wolfram Helml https://orcid.org/0000-0003-1537-2993

References

[1] Nordlund D, Ogasawara H, Bluhm H, Takahashi O, Odelius M, Nagasono M, Pettersson L G M and Nilsson A 2007 Probing the electron delocalization in liquid water and ice at attosecond time scales *Phys. Rev. Lett.* **99** 217406
[2] Sarpe C, Köhler J, Winkler T, Wollenhaupt M and Baumert T 2012 Real-time observation of transient electron density in water irradiated with tailored femtosecond laser pulses *New J. Phys.* **14** 075021
[3] Marchenko T *et al* 2018 Ultrafast nuclear dynamics in the doubly-core-ionized water molecule observed via Auger spectroscopy *Phys. Rev.* A **98** 063403
[4] Yan Z, Gray S K and Scherer N F 2014 Potential energy surfaces and reaction pathways for light-mediated self-organization of metal nanoparticle clusters *Nat. Commun.* **5** 3751
[5] Kübel M *et al* 2016 Steering proton migration in hydrocarbons using intense few-cycle laser fields *Phys. Rev. Lett.* **116** 193001
[6] Jiang L, Wang A-D, Li B, Cui T-H and Lu Y-F 2018 Electrons dynamics control by shaping femtosecond laser pulses in micro/nanofabrication: modeling, method, measurement and application *Light: Sci. Appl.* **7** 17134
[7] Seifitokaldani A *et al* 2018 Hydronium-induced switching between CO_2 electroreduction pathways *J. Am. Chem. Soc.* **140** 3833–7
[8] Ossiander M *et al* 2017 Attosecond correlation dynamics *Nat. Phys.* **13** 280–5
[9] Kelkensberg F *et al* 2011 Attosecond control in photoionization of hydrogen molecules *Phys. Rev. Lett.* **107** 043002
[10] Sainadh U S *et al* 2019 Attosecond angular streaking and tunnelling time in atomic hydrogen *Nature* **568** 75–7
[11] Grundmann S *et al* 2020 Zeptosecond birth time delay in molecular photoionization *Science* **370** 339
[12] Bakulin A A, Rao A, Pavelyev V G, van Loosdrecht P H M, Pshenichnikov M S, Niedzialek D, Cornil J, Beljonne D and Friend R H 2012 The role of driving energy and delocalized states for charge separation in organic semiconductors *Science* **335** 1340
[13] Jailaubekov A E *et al* 2013 Hot charge-transfer excitons set the time limit for charge separation at donor/acceptor interfaces in organic photovoltaics *Nat. Mater.* **12** 66–73
[14] Kastl C, Karnetzky C, Karl H and Holleitner A W 2015 Ultrafast helicity control of surface currents in topological insulators with near-unity fidelity *Nat. Commun.* **6** 6617
[15] Karnetzky C, Zimmermann P, Trummer C, Duque Sierra C, Wörle M, Kienberger R and Holleitner A 2018 Towards femtosecond on-chip electronics based on plasmonic hot electron nano-emitters *Nat. Commun.* **9** 2471
[16] Grossman M, Born B, Heyden M, Tworowski D, Fields G B, Sagi I and Havenith M 2011 Correlated structural kinetics and retarded solvent dynamics at the metalloprotease active site *Nat. Struct. Mol. Biol.* **18** 1102–8
[17] Slocik J M, Dennis P B, Govorov A O, Bedford N M, Ren Y and Naik R R 2020 Chiral restructuring of peptide enantiomers on gold nanomaterials *ACS Biomater. Sci. Eng.* **6** 2612–20
[18] Alizadeh E and Sanche L 2012 Precursors of solvated electrons in radiobiological physics and chemistry *Chem. Rev.* **112** 5578–602
[19] Orlando T M, Oh D, Chen Y and Aleksandrov A B 2008 Low-energy electron diffraction and induced damage in hydrated DNA *J. Chem. Phys.* **128** 195102
[20] Ma J, Wang F, Denisov S A, Adhikary A and Mostafavi M 2017 Reactivity of prehydrated electrons toward nucleobases and nucleotides in aqueous solution *Sci. Adv.* **3** e1701669

[21] Khan I, Tang E and Arany P 2015 Molecular pathway of near-infrared laser phototoxicity involves ATF-4 orchestrated ER stress *Sci. Rep.* **5** 10581
[22] dos Santos A F, de Almeida D R Q, Terra L F, Baptista M S and Labriola L 2019 Photodynamic therapy in cancer treatment–an update review *J. Cancer Metastasis Treat.* **5** 25
[23] Paganetti H 2012 Assessment of the risk for developing a second malignancy from scattered and secondary radiation in radiation therapy *Health Phys.* **103** 652–61
[24] Mattei I *et al* 2017 Secondary radiation measurements for particle therapy applications: prompt photons produced by ^{4}He, ^{12}C and ^{16}O ion beams in a PMMA target *Phys. Med. Biol.* **62** 1438–55
[25] Hellmann S, Rossnagel K, Marczynski-Bühlow M and Kipp L 2009 Vacuum space-charge effects in solid-state photoemission *Phys. Rev.* B **79** 035402
[26] Uhlig J, Wahlström C-G, Walczak M, Sundström V and Fullagar W 2011 Laser generated 300 keV electron beams from water *Laser Part. Beams* **29** 415–24
[27] Zhavoronkov N, Andreev A and Platonov K 2013 Sub-femtosecond hard X-ray radiation generated by electron bunches ejected from water jet *Laser Part. Beams* **31** 635–42
[28] Ammosov M V 1991 Influence of the Coulomb repulsion between electrons on their energy spectrum in the case of the nonlinear surface photoeffect *J. Opt. Soc. Am.* B **8** 2260–4
[29] Jolly W L, Bomben K D and Eyermann C J 1984 Core-electron binding energies for gaseous atoms and molecules *At. Data Nucl. Data Tables* **31** 433–93
[30] Bruch R, Luken W L, Culberson J C and Chung K T 1985 *K*-shell binding energies of B and C *Phys. Rev.* A **31** 503–4
[31] Santos J P, Parente F and Kim Y-K 2003 Cross sections for K-shell ionization of atoms by electron impact *J. Phys. B: At. Mol. Opt. Phys.* **36** 4211–24
[32] Wagner M S 2018 Advancements of attosecond photoelectron spectroscopy–streaking spectroscopy in the liquid phase and X-ray pulse characterization *PhD Thesis* Technische Universität München
[33] Corkum P B, Burnett N H and Brunel F 1989 Above-threshold ionization in the long-wavelength limit *Phys. Rev. Lett.* **62** 1259–62
[34] Faubel M, Schlemmer S and Toennies J P 1988 A molecular beam study of the evaporation of water from a liquid jet *Z. Phys.* D **10** 269–77
[35] Keldysh L V 1965 Ionization in the field of a strong electromagnetic wave *Sov. Phys - JETP* **20** 1307–14
[36] Banna M S, McQuaide B H, Malutzki R and Schmidt V 1986 The photoelectron spectrum of water in the 30 to 140 eV photon energy range *J. Chem. Phys.* **84** 4739–44
[37] Winter B, Weber R, Widdra W, Dittmar M, Faubel M and Hertel I V 2004 Full valence band photoemission from liquid water using EUV synchrotron radiation *J. Phys. Chem.* A **108** 2625–32
[38] Delone N B and Krainov V P 1998 Tunneling and barrier-suppression ionization of atoms and ions in a laser radiation field *Phys.-Usp.* **41** 469–85
[39] Tong X M and Lin C D 2005 Empirical formula for static field ionization rates of atoms and molecules by lasers in the barrier-suppression regime *J. Phys. B: At. Mol. Opt. Phys.* **38** 2593
[40] Hu S X and Keitel C H 2001 Dynamics of multiply charged ions in intense laser fields *Phys. Rev.* A **63** 053402
[41] Song M-Y, Cho H, Karwasz G P, Kokoouline V, Nakamura Y, Tennyson J, Faure A, Mason N J and Itikawa Y 2021 Cross sections for electron collisions with H_2O *J. Phys. Chem. Ref. Data* **50** 23103